Eur. Phys. J. D **60**, 309–316 (2010)
DOI: 10.1140/epjd/e2010-00192-6

THE EUROPEAN PHYSICAL JOURNAL D

Regular Article

Extreme-ultraviolet emissivity from Xe^{8+} to Xe^{12+} by using a detailed line-by-line method

J. Zeng[a], C. Gao, and J. Yuan

Department of Physics, College of Science, National University of Defense Technology, Changsha Hunan 410073, P.R. China

Received 17 December 2009 / Received in final form 4 May 2010
Published online 27 July 2010 –

Abstract. A theoretical model has been developed to calculate the emissivity of low density xenon plasmas (from Xe^{8+} to Xe^{12+}) by employing a detailed line accounting formalism. A complete set of atomic data such as transition probabilities for electric (magnetic) dipole and quadruple E1, E2, M1 and M2 and electron impact excitation collision strength, which is accurate to fine-structure level, was calculated using a full configuration interaction formalism and was used to solve the rate equation which determines the population of different levels. Detailed results are given for pure Xe^{10+} ion, which is essential for extreme-ultraviolet emission at 13.5 nm, and for low density plasmas (the electron density was taken to be 10^{12} cm^{-3}) at temperatures of 30, 45, 55, 65 and 75 eV. The fraction of different ionization stages was obtained by a completely coupled rate equation from neutral atom to Xe^{20+} by using a detailed configuration accounting method. The results show that the emissivity of the dipole forbidden lines of transition array $4s^24p^64d^75s \rightarrow 4s^24p^64d^8$ of Xe^{10+} is very sensitive to the temperature, which should be a useful tool to diagnose the temperature in EBIT plasmas.

1 Introduction

The search for optimum radiation source emitting at 13.5 nm for extreme ultraviolet (EUV) lithography is one of the most important subjects in the microelectronics industry [1]. Xenon is a popular material which can be used for EUV sources due to its inherent cleanliness and moderate conversion efficiency. Experimental research was carried out to investigate the emission properties of xenon plasmas [2–6], which showed that emission lines around 13.5 nm is mainly contributed by Xe^{10+}. Combining with theoretical analysis, researchers identified that the lines around 13.5 nm are almost entirely made up of the main $4p^64d^75p \rightarrow 4p^64d^8$ Xe^{10+} transition. Some of the experimental data such as energy levels and ionization potentials of different ionization stages of xenon are compiled by Saloman [7].

The experiments mentioned above [2–6] were performed with either laser-or gas discharge-produced plasmas with medium or high density. For such medium or high density plasmas, it is difficult to extract detailed information on atomic data of respective Xe ions due to the large number of satellite lines and/or to the limited instrumental resolution power. In order to reduce the influence of too many unresolved lines, one effective method is to further decrease the density of plasmas, resulting in fewer highly excited states and, in addition, some degree of ion stage differentiation, to gain information on emission lines of individual ion stages. Fahy et al. [8] recorded EUV spectra in the wavelength region 10–14 nm from Xe plasmas with electron densities in range of 10^{13}–10^{14} cm^{-3} or even lower than this value at the electron beam ion trap (EBIT) of NIST [9]. Later, they [10] extended their observation to the 4.5–20 nm wavelength region, with electron beam energy being varied from 180 eV to 8 keV. Radiation from charge states of Xe^{6+} to Xe^{43+} was observed. Trabert et al. [11] reported wavelengths of prominent lines arising from Li-, Be-, B-, Na-, and Mg-like ions in the 4–20 nm wavelength region using superEBIT. Biedermann et al. [12] investigated emission spectra from Xe^{17+}–Xe^{25+} in the spectral range between 9 and 25 nm using Berlin EBIT.

Various theoretical models were developed to interpret the experimental results. Sasaki et al. [13] theoretically investigated the EUV emission spectra of Xe plasma by using an unresolved transition array (UTA) model, where populations of different charge states were obtained using the WHIAM collisional-radiative (CR) model [14]. Populations of excited states were approximated to be in local thermodynamic equilibrium (LTE). Krucken et al. [15] calculated emission spectra in the optically thin limit for Xe^{8+}–Xe^{12+} at an electron density of 10^{17} cm^{-3} and an electron temperature of 32 eV based on the CR model. For EBIT plasmas, most theoretical researches used statistical approaches. Fahy et al. [8,10] calculated the wavelengths and transition probabilities for a range of charge states in xenon (Xe^{8+}–Xe^{17+}) using the Cowan suite of codes, which were used to aid experimental analysis. In

[a] e-mail: jiaolongzeng@hotmail.com

a comparison between atomic structure calculations and experiment they found that their theory overestimated the line intensity ratio at 11 nm (lines contributed by $4p^6 4d^7 4f \rightarrow 4p^6 4d^8$ and $4p^5 4d^9 \rightarrow 4p^6 4d^8$) and at 13.5 nm (by $4p^6 4d^7 5p \rightarrow 4p^6 4d^8$) by a factor close to 7. To support the identification of the observed lines, Biedermann et al. [12] utilized the HULLAC computer package [16] combined with a CR model. They pointed out that there is an increasing discrepancy between observed wavelengths and predicted values for lower charged Xe ions successively filling the $4p$ subshell. Trabert et al. [11] also suggested that there exist significant shortcomings for various theoretical predictions, which failed to agree with their precise results.

The disagreement between the theory and experiment is mainly due to the challenging treatment of the complex electron correlation. In this work, we investigate emissivity of low density plasmas (Xe^{8+}–Xe^{12+}) by using a detailed line accounting method. In order to take into account the adequate electron correlation, large-scale configuration interaction (CI) calculations were carried out to obtain as accurate atomic data as possible.

2 Theoretical method

The emissivity in a plasma is determined by all transitions including bound-bound, free-bound and free-free processes. In the present work, we only consider bound-bound emissivity using a detailed line-by-line approach. For a plasma of temperature T and electron density N_e, the emissivity at a given photon energy $h\nu$ is given by

$$\varepsilon_\nu = \sum_z \sum_{i<j} h\nu N_{zj} A_{ji} S_{ji}(h\nu), \tag{1}$$

where N_{zj} denotes the population of upper level j of charge state z, A_{ji} is the spontaneous radiative transition probability for an emission line of $j \rightarrow i$ and $S_{ji}(h\nu)$ is the corresponding line profile function, which in general should be a Voigt profile in which contributions of all broadening mechanisms are included. In this work, we assume a Gaussian line profile, where the line width is taken to be a typical experimental resolution of 0.015 nm.

In principle, the population N_{zj} for different ionization stages can be obtained by solving a complete coupled rate equation in which one takes into account of all levels of all charge states existing in the plasma. For xenon ions near Xe^{10+}, this is a challenging undertaking as there are many fine-structure levels involved in the rate equation. To make this rate equation tractable, we developed a detailed configuration accounting model to obtain the abundance of different charge states. In the steady-state assumption, the populations of the configurations are constant, due to the exact balance between the various populating and depopulating atomic processes. For each configuration i, the rate equation can be written as

$$\frac{dn_i}{dt} = \sum_{j\neq i}^{N_L} n_j R_{ji} - n_i \sum_{j\neq i}^{N_L} R_{ij} = 0, \tag{2}$$

where n_i is the population of configuration i and R_{ij} and R_{ji} represent the depopulating and populating rates between configurations i and j, respectively, and N_L is the total number of configurations included in the rate equation. The rate coefficients of five different atomic processes and their inverse processes are included in the rate equation,

$$R_{ij} = A_{ij} + B_{ij} + C_{ij} + D_{ij} + E_{ij}, \tag{3}$$

where A_{ji}, B_{ij}, C_{ij}, D_{ij} and E_{ij} represent rates for photo-excitation ($i < j$) or photo-de-excitation ($i > j$), electron collision excitation ($i < j$) or de-excitation ($i > j$), photoionization ($i < j$) or radiative recombination ($i > j$), electron collision ionization ($i < j$) or three body recombination ($i > j$), autoionization ($i < j$) or dielectronic recombination ($i > j$), respectively. For optically thin plasma, the radiation can easily escape from the plasma and thus we did not include the radiation field in this work. Therefore, we excluded the rates contributed by photo-excitation and photoionization processes stimulated by the radiation field. Yet the rates contributed by the spontaneous decay process are taken into account.

To build a reasonable atomic model, we included a large number of configurations in the rate equation. Take Xe^{10+} as an example to illustrate the size of our atomic model. The configurations included in the rate equation are (a) singly excited ones: $4s^2 4p^6 4d^8$, $4s^2 4p^6 4d^7 nl$, $4s^2 4p^5 4d^9$, $4s^2 4p^5 4d^8 nl$, $4s^1 4p^6 4d^9$, $4s^1 4p^6 4d^8 nl$; (b) doubly excited ones: $4s^2 4p^6 4d^6 4f^2$, $4s^2 4p^6 4d^6 4fnl$, $4s^2 4p^6 4d^6 5lnl'$, $4s^2 4p^4 4d^{10}$, $4s^2 4p^4 4d^9 nl$, $4s^2 4p^4 4d^8 4f^2$, $4s^2 4p^4 4d^8 4fnl$, $4s^2 4p^4 4d^8 5lnl'$, $4s^2 4p^5 4d^7 4f^2$, $4s^2 4p^5 4d^7 4fnl$, $4s^2 4p^5 4d^7 5lnl'$, $4s^1 4p^6 4d^7 4f^2$, $4s^1 4p^6 4d^7 4fnl$, $4s^1 4p^6 4d^7 5lnl'$, $4s^1 4p^5 4d^{10}$, $4s^1 4p^5 4d^9 nl$, $4s^1 4p^5 4d^8 4f^2$, $4s^1 4p^5 4d^8 4fnl$, $4s^1 4p^5 4d^8 5lnl'$, $4p^6 4d^{10}$, $4p^6 4d^9 nl$, $4p^6 4d^8 4f^2$, $4p^6 4d^8 4fnl$, $4p^6 4d^8 5lnl'$; and (c) triply excited ones: $4s^2 4p^6 4d^5 4f^3$, $4s^2 4p^6 4d^5 4f^2 nl$, $4s^2 4p^5 4d^6 4f^3$, $4s^2 4p^5 4d^6 4f^2 nl$, $4s^2 4p^4 4d^7 4f^3$, $4s^2 4p^4 4d^7 4f^2 nl$ ($n \leq 9$, $l, l' \leq 6$). The total number of the selected non-relativistic configurations is 1373 for Xe^{10+} with 54 of which are bound and 1319 are autoionized. Similar consideration applied to other xenon ions which are extended from neutral atom to Xe^{20+}. Such a size of atomic model is adequate to get converged results for the abundance distribution among different charge states. The detailed treatment of the rate coefficients required in the rate equation was similar to work reported in literature [17,18].

Better treatment should be accurate to fine-structure levels, however, such a method can easily be untractable for xenon plasma as the number of levels can easily exceed 1 000 000 for a single ion such as Xe^{10+}. Therefore, we have to reduce the number of levels in the detailed line-by-line calculation. For a particular charge state z, level

populations are obtained by solving a set of coupled rate equations

$$N_{zj}\left[\sum_{i<j}A_{ji}+n_e\left(\sum_{i<j}B^d_{ji}+\sum_{i>j}B^e_{ji}\right)\right]=\sum_{i>j}N_{zi}A_{ij}+n_e\left(\sum_{i<j}N_{zi}B^e_{ij}+\sum_{i>j}N_{zi}B^d_{ij}\right), \quad (4)$$

where the superscripts e and d refer to electron impact excitation and de-excitation rate coefficients, respectively, N_{zj} is number density of level j of charge state z, and n_e is electron density.

The excitation rate coefficients are obtained from effective electron impact collision strengths Υ_{ij}

$$B^e_{ij}=\frac{8.63\times10^{-6}}{g_iT^{1/2}}e^{-E_{ij}/kT}\Upsilon_{ij}, \quad (5)$$

where E_{ij} is energy difference between levels i and j, and g_i is statistical weight of level i. The de-excitation rate coefficients are obtained by detailed balancing. The effective collision strength can be obtained by integrating collision strength over electron velocity distribution function (a Maxwellian one is assumed here)

$$\Upsilon_{ij}=\int_0^\infty \Omega_{ij}\exp\left(-\frac{E}{kT}\right)d\left(\frac{E}{kT}\right), \quad (6)$$

where E is scattered electron energy and k is Boltzmann's constant.

It is obvious that one needs a large number of atomic data such as energy levels, radiative transition probability (including E1, E2, M1 and M2 transitions) and electron impact excitation cross sections (collision strengths) to calculate the emission spectra. The calculations of atomic structure and electron impact excitation collision strength have been carried out using flexible atomic code (FAC) developed by Gu [19]. A fully relativistic approach based on the Dirac equation is used throughout the entire package. In the calculation of atomic structure, the energy levels of an atomic ion are obtained by diagonalizing the relativistic Hamiltonian. The radial orbits are derived from a modified Dirac-Fock-Slater iteration on a fictitious mean configuration with fractional occupation numbers, representing the average electron cloud of the configurations included in the calculation. The electron impact excitation collision strength has been calculated using a relativistic distorted-wave approximation. To ensure convergence of the collision strengths, large angular momentum contributions have been explicitly taken into account. Higher partial wave contributions have been included using the Coulomb-Bethe approximation [20].

The favorable plasma condition for EUV emission at 13.5 nm should be that Xe^{10+} has the largest fraction, therefore we focused on xenon ions from Xe^{8+} to Xe^{12+}. The structure of these ions are very complex and many physical effects, in particular CI, play important roles in obtaining accurate atomic data. To have a quantitative understanding of the calculation scale, we take Xe^{10+} as an example. In the calculation of energy levels, transition probability and electron impact excitation collision strengths, we included interactions between following configurations: $4s^24p^64d^8$, $4s^24p^64d^74f$, $4s^24p^64d^75l$, $4s^24p^54d^9$, $4s^24p^54d^84f$, $4s^24p^54d^85l$ (l = s, p, d), $4s^24p^64d^64f^2$, $4s^24p^64d^64f5s$, $4s^24p^64d^64f5p$, $4s^24p^64d^65s^2$, $4s^24p^64d^65s5p$, $4s^24p^64d^65p^2$, $4s^24p^64d^54f^3$, $4s^24p^44d^{10}$, and $4s^24p^54d^74f^2$ in the detailed line-by-line calculation. We chose the above configurations in our calculation because main electron correlations have been included for Xe^{10+} ion. Trial computations were carried out and it was found that $4p^2$–$4d^2$ and $4d^2$–$4f^2$ correlations are very important and should be taken into account to obtain as accurate atomic data as possible. All above configurations lead to 22 170 levels in total. In order to take enough cascade effects from higher levels into account and simultaneously, to keep the calculation tractable, we restricted our computation of electron impact excitation collision strength, which is the most time consuming among the above mentioned physical processes, among the lowest 800 levels. Calculations with similar sizes were carried out for other charge states.

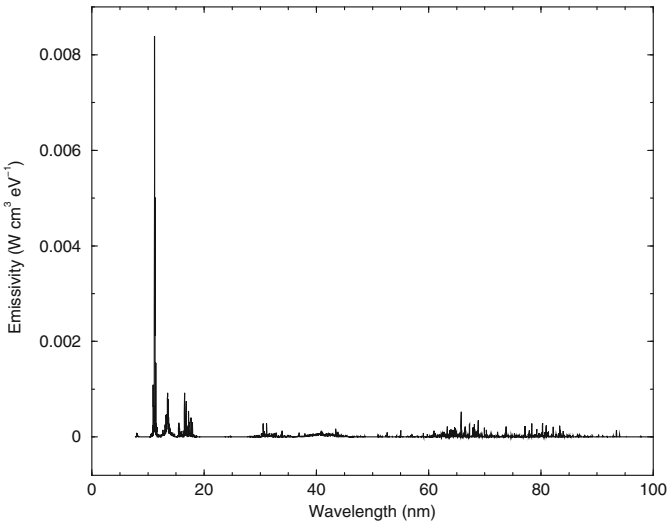

Fig. 1. An overview of emissivity of Xe^{10+} in a wavelength range of 7–100 nm at a temperature of 55 eV and an electron density of 10^{12} cm^{-3}.

3 Results and discussion

As mentioned in the introduction, EUV emission lines at 13.5 nm are predominantly contributed by Xe^{10+}, therefore, it is helpful to first investigate its emission property. Let us assume a plasma in which only Xe^{10+} exists. Figure 1 shows an overview of its emissivity in the wavelength range 7–100 nm at a temperature of 55 eV and an electron density of 10^{12} cm^{-3} (which is a typical value for EBIT plasmas and hence we assume this density throughout this

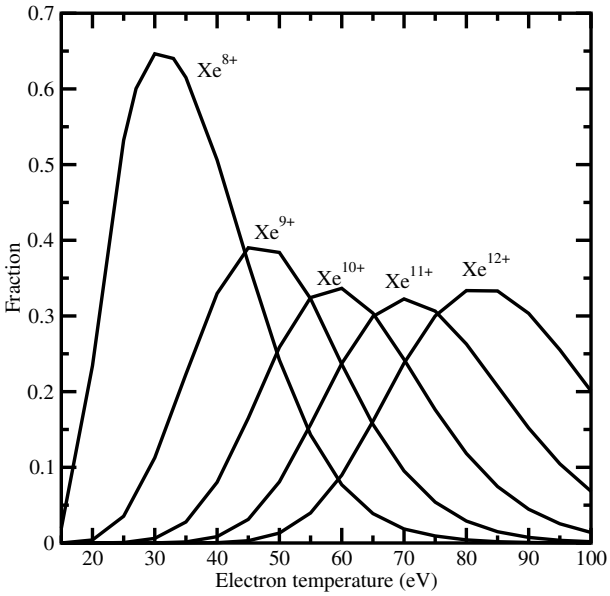

Fig. 2. The fraction of Xe^{8+}–Xe^{12+} charge states as a function of temperature at an electron density of 10^{12} cm^{-3}.

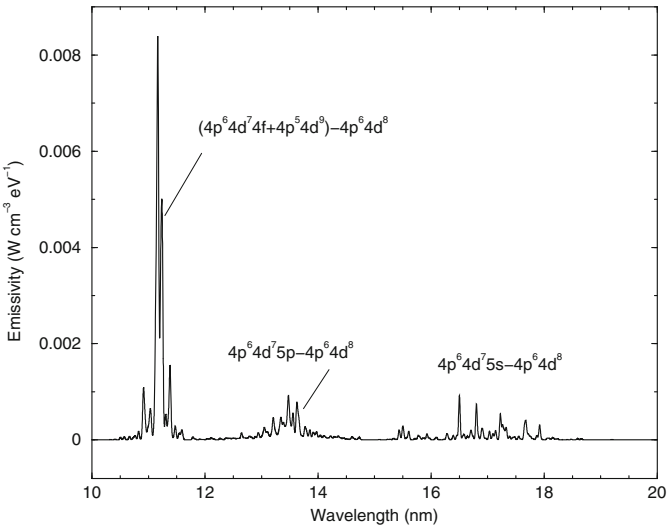

Fig. 3. Emissivity of Xe^{10+} at temperature of 55 eV in wavelength region of 10–20 nm. The electron density is taken to be 10^{12} cm^{-3}.

paper). We chose 55 eV because at this temperature Xe^{10+} is the most abundant ion at such a physical condition according to the rate equation. As illustrative examples, Figure 2 shows the fraction of Xe^{8+}–Xe^{12+} as a function of temperature. To obtain this result, we included ionization stages from neutral atom to Xe^{20+}, as mentioned in the above. At each temperature, 12 successive charge states were included in a rate equation to ensure the convergence. To save space, the fraction of other ionization stages were not given in Figure 2. It can be seen that the temperature of peak abundance for Xe^{8+}–Xe^{12+} is 30, 45, 55, 65 and 75 eV, respectively. The maximal abundance for Xe^{8+} is much larger than other xenon ions, which is mainly due to its full electronic structure. The ground configuration of Xe^{8+}–Xe^{12+} is $4s^24p^64d^m$ (m = 10,9,8,7,6), respectively. Only Xe^{8+} has a full subshell ground configuration of $4s^24p^64d^{10}$.

From the inspection of Figure 1, one can see that Xe^{10+} emits strong lines mainly at 10–20 and 60–90 nm regions. The lines at 60–90 nm regions originate dominantly from E2 and M1 transitions between levels of the ground configuration $4s^24p^64d^8$ and between levels of the first excited one $4s^24p^64d^75s$. For lines below 20 nm, the strong emission lines near 11 nm originate from E1 transitions of $4s^24p^64d^74f \rightarrow 4s^24p^64d^8$ and $4s^24p^54d^9 \rightarrow 4s^24p^64d^8$ and lines at 13.5 nm from $4s^24p^64d^75p \rightarrow 4s^24p^64d^8$, while those near 17 nm are contributed by the dipole forbidden transitions of $4s^24p^64d^75s \rightarrow 4s^24p^64d^8$.

Below we focus our attention on the strong lines in region of 10–20 nm. The emissivity of Xe^{10+} in the region 10–20 nm was redrawn in Figure 3 at the temperature of 55 eV in an expanded scale. The emission lines around 13.5 nm are evident in the plot, which are relevant to the EUV lithography. It is useful to identify the origin of the spectral lines shown in Figure 3.

Table 1 lists the upper and lower level designation, wavelength and relative intensity ratio of some strong lines to the strongest line $((4d_{5/2}^{-3})_{9/2}4f_{7/2})_5 \rightarrow (4d_{5/2}^{-2})_4$ (which is normalized to unity). It appears that there are many more strong emission lines near 11 nm than those shown in Figure 3, however, some of them are so close that they coalesce together and looks like one individual line. For example, the strongest line originates from $((4d_{5/2}^{-3})_{9/2}4f_{7/2})_5 \rightarrow (4d_{5/2}^{-2})_4$ which is located at 11.163 nm. Near this line, there are at least 7 spectral lines which are indistinguishable from each other in the figure: $((4d_{3/2}^{-1}(4d_{5/2}^{-2})_4)_{9/2}4f_{7/2})_3$ (368) $\rightarrow$ $(4d_{3/2}^{-1}4d_{5/2}^{-1})_3$ (2) at 11.151 nm, $((4d_{3/2}^{-1}(4d_{5/2}^{-2})_4)_{9/2}4f_{7/2})_3$ (368) $\rightarrow$ $(4d_{5/2}^{-2})_2$ (3) at 11.154 nm, $((4d_{3/2}^{-1}(4d_{5/2}^{-2})_4)_{5/2}4f_{7/2})_1$ (403) $\rightarrow$ $(4d_{3/2}^{-1}4d_{5/2}^{-1})_1$ (6) at 11.159 nm, $((4d_{3/2}^{-1}(4d_{5/2}^{-2})_4)_{9/2}4f_{7/2})_2$ (383) $\rightarrow$ $(4d_{3/2}^{-1}4d_{5/2}^{-1})_2$ (4) at 11.166 nm, $(4p_{3/2}^{-1}4d_{5/2}^{-1})_2$ (366) $\rightarrow$ $(4d_{5/2}^{-2})_2$ (3) at 11.166 nm, $(((4d_{3/2}^{-2})_2 4d_{5/2}^{-1})_{9/2}4f_{5/2})_4$ (364) $\rightarrow$ $(4d_{3/2}^{-1}4d_{5/2}^{-1})_3$ (2) at 11.170 nm, and $(((4d_{3/2}^{-2})_2 4d_{5/2}^{-1})_{1/2}4f_{5/2})_3$ (382) $\rightarrow$ $(4d_{3/2}^{-1}4d_{5/2}^{-1})_2$ (4) at 11.174 nm. In level designation, $4d_{3/2}^{-1}$ or $4d_{5/2}^{-1}$ indicates a hole in the respective subshell. The number in the parentheses denotes the labeling sequence of the corresponding level in the full level list. Many lines are merged together and indistinguishable, resulting in the difficulty in obtaining information of respective level. Compared with the strong lines of $4f \rightarrow 4d$ and $4d \rightarrow 4p$ near 11 nm, the lines around 13.5 nm originating from $5p \rightarrow 4d$ are much weaker. In EUV lithography, strong emission around 13.5 nm is required. Further investigation shows that the relative intensity is very sensitive to the temperature for the dipole forbidden lines, while it is insensitive for the dipole allowed ones. Such a characteristic should be a useful tool for temperature diagnosis.

Table 1. Level designation (j and i represent the number sequence in the whole level list), angular momentum, wavelength λ (nm) and relative intensity for prominent spectral lines of Xe^{10+} at temperature of 55 eV. The strongest line at 11.1628 (355 → 1) is normalized to unity. In level designation, $4p_{1/2}^{-1}$, $4d_{3/2}^{-1}$ and $4d_{5/2}^{-1}$ indicate a hole in the respective subshell and full subshells are omitted.

Upper (j)	Upper J	Lower (i)	Lower J	λ (nm)	Relative intensity
$4p_{1/2}^{-1}4d_{5/2}^{-1}$ (466)	3	$4d_{3/2}^{-1}4d_{5/2}^{-1}$ (7)	4	10.909	0.332
$4p_{1/2}^{-1}4d_{5/2}^{-1}$ (446)	2	$4d_{3/2}^{-1}4d_{5/2}^{-1}$ (6)	1	10.940	0.109
$4p_{1/2}^{-1}4d_{5/2}^{-1}$ (446)	2	$4d_{3/2}^{-2}$ (8)	2	11.024	0.132
$((4d_{3/2}^{-2})_2 4d_{5/2}^{-1})_{5/2}4f_{7/2}$ (517)	1	$4d_{3/2}^{-2}$ (9)	0	11.117	0.104
$((4d_{3/2}^{-2})_2 4d_{5/2}^{-1})_{9/2}4f_{7/2}$ (423)	2	$4d_{3/2}^{-2}$ (8)	2	11.132	0.153
$((4d_{3/2}^{-2})_2 4d_{5/2}^{-1})_{9/2}4f_{7/2}$ (419)	5	$4d_{3/2}^{-1}4d_{5/2}^{-1}$ (7)	4	11.132	0.667
$(4d_{3/2}^{-1}(4d_{5/2}^{-2})_4)_{9/2}4f_{7/2}$ (368)	3	$4d_{3/2}^{-1}4d_{5/2}^{-1}$ (2)	3	11.151	0.204
$(4d_{3/2}^{-1}(4d_{5/2}^{-2})_4)_{9/2}4f_{7/2}$ (368)	3	$4d_{5/2}^{-2}$ (3)	2	11.154	0.259
$(4d_{3/2}^{-1}(4d_{5/2}^{-2})_4)_{5/2}4f_{7/2}$ (403)	1	$4d_{3/2}^{-1}4d_{5/2}^{-1}$ (6)	1	11.159	0.117
$(4d_{5/2}^{-3})_{9/2}4f_{7/2}$ (355)	5	$4d_{5/2}^{-2}$ (1)	4	11.163	1.000
$(4d_{3/2}^{-1}(4d_{5/2}^{-2})_4)_{9/2}4f_{7/2}$ (383)	2	$4d_{3/2}^{-1}4d_{5/2}^{-1}$ (4)	2	11.166	0.262
$4p_{3/2}^{-1}4d_{5/2}^{-1}$ (366)	2	$4d_{5/2}^{-2}$ (3)	2	11.166	0.265
$((4d_{3/2}^{-2})_2 4d_{5/2}^{-1})_{9/2}4f_{5/2}$ (364)	4	$4d_{3/2}^{-1}4d_{5/2}^{-1}$ (2)	3	11.170	0.624
$((4d_{3/2}^{-2})_2 4d_{5/2}^{-1})_{1/2}4f_{5/2}$ (382)	3	$4d_{3/2}^{-1}4d_{5/2}^{-1}$ (4)	2	11.174	0.412
$(4d_{3/2}^{-1}(4d_{5/2}^{-2})_2)_{11/2}4f_{5/2}$ (354)	3	$4d_{5/2}^{-2}$ (1)	4	11.213	0.543
$(4d_{3/2}^{-1}(4d_{5/2}^{-2})_2)_{9/2}4f_{7/2}$ (361)	3	$4d_{3/2}^{-1}4d_{5/2}^{-1}$ (2)	3	11.217	0.238
$(4d_{3/2}^{-1}(4d_{5/2}^{-2})_2)_{9/2}4f_{7/2}$ (361)	3	$4d_{5/2}^{-2}$ (3)	2	11.220	0.206
$((4d_{3/2}^{-2})_2 4d_{5/2}^{-1})_{9/2}4f_{5/2}$ (359)	2	$4d_{3/2}^{-1}4d_{5/2}^{-1}$ (2)	3	11.232	0.225
$((4d_{3/2}^{-2})_0 4d_{5/2}^{-1})_{5/2}4f_{7/2}$ (389)	1	$4d_{5/2}^{-2}$ (5)	0	11.238	0.112
$(4d_{3/2}^{-3})_{3/2}4f_{5/2}$ (405)	3	$4d_{3/2}^{-2}$ (8)	2	11.242	0.322
$(4d_{5/2}^{-3})_{9/2}4f_{7/2}$ (353)	4	$4d_{5/2}^{-2}$ (1)	4	11.245	0.792
$(4d_{3/2}^{-1}(4d_{5/2}^{-2})_2)_{7/2}4f_{5/2}$ (356)	1	$4d_{5/2}^{-2}$ (3)	2	11.306	0.163
$(4d_{3/2}^{-1}(4d_{5/2}^{-2})_4)_{11/2}4f_{7/2}$ (380)	4	$4d_{3/2}^{-1}4d_{5/2}^{-1}$ (7)	4	11.381	0.496
$(4d_{3/2}^{-1}(4d_{5/2}^{-2})_4)_{11/2}5s_{1/2}$ (25)	6	$4d_{5/2}^{-2}$ (1)	4	16.501	0.140

Figures 4 shows the emissivity of Xe^{8+}, Xe^{9+}, Xe^{11+} and Xe^{12+} at temperature of 30, 45, 65 and 75 eV in wavelength region of 9–23 nm. We chose these temperatures for the respective ions because they have the largest fraction under such physical conditions, which can easily be seen from Figure 2. It was found that the emission characteristics is rather different for different ion. For Xe^{8+}, there are only five strong lines in the shown wavelength range. The strongest one located at 12.099 nm originates from $4s^24p^6(4d_{5/2}^{-1}4f_{7/2})_1 \rightarrow 4s^24p^64d^{10}$. The next strongest lines located at 21.104 and 21.898 nm originate from the dipole forbidden transitions of $4s^24p^6(4d_{5/2}^{-1}5s_{1/2})_2 \rightarrow 4s^24p^64d^{10}$ and $4s^24p^6(4d_{3/2}^{-1}5s_{1/2})_2 \rightarrow 4s^24p^64d^{10}$, respectively. A combination of two lines at 15.515 nm and 15.526 nm is due to $4s^24p^6(4d_{5/2}^{-1}4f_{5/2})_1 \rightarrow 4s^24p^64d^{10}$ and $4s^24p^6(4d_{3/2}^{-1}5p_{1/2})_1 \rightarrow 4s^24p^64d^{10}$). The weaker line at 15.230 nm originates from $4s^24p^6(4d_{5/2}^{-1}5p_{3/2})_1 \rightarrow 4s^24p^64d^{10}$. The strongest line $4s^24p^6(4d_{5/2}^{-1}4f_{7/2})_1 \rightarrow 4s^24p^64d^{10}$ and the dipole forbidden lines of $4s^24p^6(4d_{3/2}^{-1}5s_{1/2})_2 \rightarrow 4s^24p^64d^{10}$ and $4s^24p^6(4d_{5/2}^{-1}5s_{1/2})_2 \rightarrow 4s^24p^64d^{10}$ of Xe^{8+} is not merged with other lines, and therefore it can be used as an indicator of plasma condition. For Xe^{9+}, however, there are many more emission lines than Xe^{8+}. Besides the emission lines $4f \rightarrow 4d$ (located at 11–12 nm) and $5p \rightarrow 4d$ (at 14.4–15.6 nm), there are strong dipole forbidden lines originating from transition of $5s \rightarrow 4d$ (17–19 nm). The wavelength of the dipole forbidden lines $5s \rightarrow 4d$ for Xe^{8+} are much larger than those of Xe^{9+}. The energy of levels belonging to the configuration of $4s^24p^64d^85s$ are lower

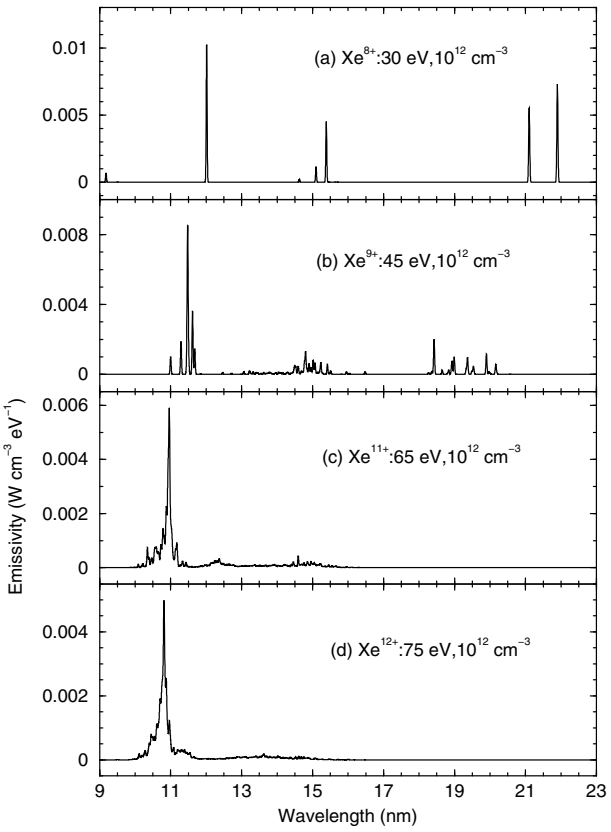

Fig. 4. Emissivity of Xe^{8+}, Xe^{9+}, Xe^{11+} and Xe^{12+} in region of 9–23 nm at electron density of 10^{12} cm^{-3}. The temperature corresponds to the most abundance of respective ion.

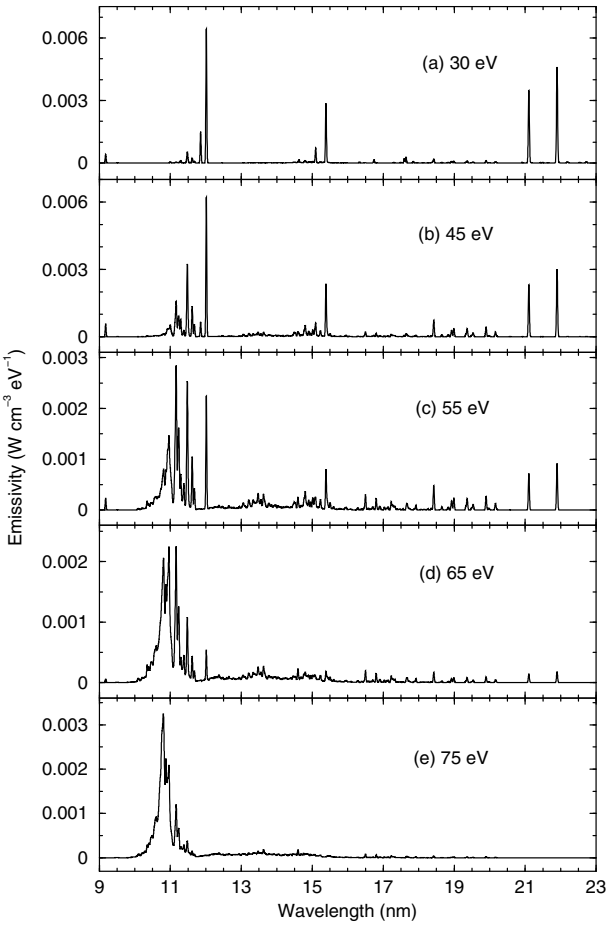

Fig. 5. Emissivity of xenon plasmas at temperature of 30, 45, 55, 65 and 75 eV in wavelength region of 9–23 nm. The electron density is taken to be 10^{12} cm^{-3}.

than those of $4s^24p^64d^85p$ and $4s^24p^64d^84f$, and therefore the levels of $4s^24p^64d^85s$ are metastable. A similar conclusion is applicable to Xe^{8+} and Xe^{10+}. Moving to Xe^{11+} and Xe^{12+}, the levels of $4s^24p^64d^m5s$ are no longer metastable and therefore the corresponding lines disappeared in Figures 4c and 4d. Furthermore, the intensity of $5p \rightarrow 4d$ lines are weaker and weaker with the increase of the ionization stages.

Now let us turn to the real plasmas with abundance of different charge states being determined by the coupled rate equation. Figure 5 shows the emissivity of xenon plasmas at temperature of 30, 45, 55, 65 and 75 eV. The contributions to the emissivity of ionization stages from Xe^{5+} to Xe^{16+} were considered. For example, at the temperature of 30 eV, the fractions of Xe^{5+}–Xe^{11+} are 0.16%, 8.03%, 13.01%, 62.04%, 15.34%, 1.36% and 0.06%, respectively. At the temperature of 75 eV, the fractions of Xe^{8+}–Xe^{16+} are 0.28%, 1.99%, 8.69%, 22.33%, 35.72%, 21.48%, 7.46%, 1.84%, and 0.22%, respectively. Therefore we performed calculations by explicitly including ionization stages of Xe^{5+}–Xe^{11+} and Xe^{8+} to Xe^{16+} at the temperatures of 30 and 75 eV, respectively. The feature of spectral lines differs considerably with the increase of temperature. Such a sensitivity is basically due to the sensitivity of abundance of different charge states to the temperature. At 30 eV, the dominant ion type is Xe^{8+} (62%). As mentioned above, Xe^{8+} has a full electron structure and the number of emission lines is sparse. As discussed in the above, the strong lines at ∼12.1, 15.4, 21.1 and 21.9 nm originate from Xe^{8+}. When the temperature is increased to 45 and 55 eV, the spectrum shows richer line structures, many of which are contributed by Xe^{10+}. With a further increase of temperature, the emission lines from $5p \rightarrow 4d$ and $5s \rightarrow 4d$ at wavelength region of 13–20 nm are becoming weaker and weaker. Such a characteristic is a consequence of atomic structure of the relevant ions. As shown in the above, for Xe^{8+}–Xe^{10+}, the energically lowest excited configuration of $4s^24p^64d^m5s$ (m = 9, 8, 7 respectively) is metastable because there are no dipole allowed channels to decay to lower levels. The levels belonging to configuration of $4s^24p^64d^m5s$ are more abundant than other higher excited levels which can decay to lower levels via dipole transitions. As a result, there are strong dipole forbidden lines in the emission spectrum for these ions. For higher ionization stages such as Xe^{11+}, however, the levels belonging to configuration of $4s^24p^54d^8$ are energetically lower than those of $4s^24p^64d^65s$, resulting in no strong dipole forbidden transitions in the emission spectrum. Moreover, with the increasing of ionization stage, the contributions to emissivity from $5p$–$4d$ transitions reduce for Xe^{11+} and

Table 2. Emissivity (in unit of 1.0×10^{-4} W cm^{-3}) of prominent spectral lines of xenon plasmas at temperature of 30, 45, 55, and 65 eV.

Ion stage	Upper	Upper J	Lower	Lower J	λ (nm)	30 eV	45 eV	55 eV	65 eV
Xe^{8+}	$4d_{5/2}^{-1}4f_{7/2}$	1	$4d^{10}$	0	12.015	17.5	17.2	5.6	
	$4d_{5/2}^{-1}4f_{5/2}$	1	$4d^{10}$	0	15.377	0.88	0.65	0.20	
	$4d_{3/2}^{-1}5p_{1/2}$	1	$4d^{10}$	0	15.387	4.1	3.5	1.0	
	$4d_{3/2}^{-1}5s_{1/2}$	2	$4d^{10}$	0	21.104	3.6	2.5	0.7	
	$4d_{5/2}^{-1}5s_{1/2}$	2	$4d^{10}$	0	21.898	4.5	3.0	0.8	
Xe^{9+}	$4p_{1/2}^{-1}$	1/2	$4d_{3/2}^{-1}$	3/2	10.999	0.21	1.3	1.0	
	$4p_{3/2}^{-1}$	3/2	$4d_{5/2}^{-1}$	5/2	11.292	0.38	2.4	1.8	
	$(4d_{3/2}^{-1})_2 4f_{5/2}$	3/2	$4d_{5/2}^{-1}$	5/2	11.458	0.14	0.88	0.65	
	$(4d_{5/2}^{-1})_2 4f_{7/2}$	7/2	$4d_{5/2}^{-1}$	5/2	11.477	1.1	6.6	4.9	
	$(4d_{3/2}^{-1})_2 4f_{5/2}$	5/2	$4d_{3/2}^{-1}$	3/2	11.483	0.64	3.9	2.9	
	$4p_{3/2}^{-1}$	3/2	$4d_{3/2}^{-1}$	3/2	11.508	0.14	0.91	0.68	
	$(4d_{5/2}^{-1})_4 4f_{7/2}$	5/2	$4d_{5/2}^{-1}$	5/2	11.617	0.72	4.4	3.3	
	$(4d_{3/2}^{-1})_2 4f_{5/2}$	3/2	$4d_{3/2}^{-1}$	3/2	11.679	0.29	1.8	1.3	
	$(4d_{3/2}^{-1}4d_{5/2}^{-1})_4 5s_{1/2}$	9/2	$4d_{5/2}^{-1}$	5/2	18.424	2.4	1.0	0.64	
Xe^{10+}	$4p_{1/2}^{-1}4d_{5/2}^{-1}$	3	$4d_{3/2}^{-1}4d_{5/2}^{-1}$	4	10.909		0.60	1.0	0.75
	$4p_{1/2}^{-1}4d_{5/2}^{-1}$	2	$4d_{3/2}^{-2}$	2	11.024		0.24	0.41	0.3
	$((4d_{3/2}^{-2})_2 4d_{5/2}^{-1})_{5/2}4f_{7/2}$	1	$4d_{3/2}^{-2}$	0	11.117		0.19	0.33	0.24
	$((4d_{3/2}^{-2})_2 4d_{5/2}^{-1})_{9/2}4f_{7/2}$	2	$4d_{3/2}^{-2}$	2	11.132		0.28	0.48	0.34
	$((4d_{3/2}^{-2})_2 4d_{5/2}^{-1})_{9/2}4f_{7/2}$	5	$4d_{3/2}^{-1}4d_{5/2}^{-1}$	4	11.132		1.2	2.0	1.5
	$(4d_{3/2}^{-1}(4d_{5/2}^{-2})_4)_{9/2}4f_{7/2}$	3	$4d_{3/2}^{-1}4d_{5/2}^{-1}$	3	11.151		0.38	0.64	0.45
	$(4d_{3/2}^{-1}(4d_{5/2}^{-2})_4)_{9/2}4f_{7/2}$	3	$4d_{5/2}^{-2}$	2	11.154		0.48	0.81	0.58
	$(4d_{3/2}^{-1}(4d_{5/2}^{-2})_4)_{5/2}4f_{7/2}$	1	$4d_{3/2}^{-1}4d_{5/2}^{-1}$	1	11.159		0.22	0.37	0.26
	$(4d_{5/2}^{-3})_{9/2}4f_{7/2}$	5	$4d_{5/2}^{-2}$	4	11.163		1.8	3.1	2.2
	$(4d_{3/2}^{-1}(4d_{5/2}^{-2})_4)_{9/2}4f_{7/2}$	2	$4d_{3/2}^{-1}4d_{5/2}^{-1}$	2	11.166		0.49	0.82	0.58
	$4p_{3/2}^{-1}4d_{5/2}^{-1}$	2	$4d_{5/2}^{-2}$	2	11.166		0.49	0.83	0.59
	$((4d_{3/2}^{-2})_2 4d_{5/2}^{-1})_{9/2}4f_{5/2}$	4	$4d_{3/2}^{-1}4d_{5/2}^{-1}$	3	11.170		1.2	2.0	1.4
	$((4d_{3/2}^{-2})_2 4d_{5/2}^{-1})_{1/2}4f_{5/2}$	3	$4d_{3/2}^{-1}4d_{5/2}^{-1}$	2	11.174		0.76	1.3	0.92
	$(4d_{3/2}^{-1}(4d_{5/2}^{-2})_2)_{11/2}4f_{5/2}$	3	$4d_{5/2}^{-2}$	4	11.213		0.99	1.7	1.2
	$(4d_{3/2}^{-1}(4d_{5/2}^{-2})_2)_{9/2}4f_{7/2}$	3	$4d_{3/2}^{-1}4d_{5/2}^{-1}$	3	11.217		0.44	0.75	0.53
	$(4d_{3/2}^{-1}(4d_{5/2}^{-2})_2)_{9/2}4f_{7/2}$	3	$4d_{5/2}^{-2}$	2	11.220		0.38	0.64	0.46
	$((4d_{3/2}^{-2})_2 4d_{5/2}^{-1})_{9/2}4f_{5/2}$	2	$4d_{3/2}^{-1}4d_{5/2}^{-1}$	3	11.232		0.42	0.70	0.50
	$((4d_{3/2}^{-2})_0 4d_{5/2}^{-1})_{5/2}4f_{7/2}$	1	$4d_{5/2}^{-2}$	0	11.238		0.21	0.35	0.25
	$(4d_{3/2}^{-3})_{3/2}4f_{5/2}$	3	$4d_{3/2}^{-2}$	2	11.242		0.59	1.0	0.72
	$(4d_{5/2}^{-3})_{9/2}4f_{7/2}$	4	$4d_{5/2}^{-2}$	4	11.245		1.5	2.5	1.8
	$(4d_{3/2}^{-1}(4d_{5/2}^{-2})_2)_{7/2}4f_{5/2}$	1	$4d_{5/2}^{-2}$	2	11.306		0.30	0.51	0.36
	$(4d_{3/2}^{-1}(4d_{5/2}^{-2})_4)_{11/2}4f_{7/2}$	4	$4d_{3/2}^{-1}4d_{5/2}^{-1}$	4	11.381		0.91	1.6	1.1
	$(4d_{3/2}^{-1}(4d_{5/2}^{-2})_4)_{11/2}5s_{1/2}$	6	$4d_{5/2}^{-2}$	4	16.501		0.30	0.44	0.28

higher ionization stages. Therefore, the spectrum shows strong emission only around 11 nm, which is caused by $4f \rightarrow 4d$ and $4d \rightarrow 4p$ transitions. The emissivity of the prominent spectral lines of xenon plasmas at temperature of 30, 45, 55, and 65 eV are listed in Table 2, where the meaning of level designation and angular momentum for the upper and lower levels is the same as in Table 1. The line merging for Xe^{11+} and Xe^{12+} is too strong to be given. For example, all strong lines for Xe^{11+} and Xe^{12+} are located in region of 10.2–11.5 nm. Some of the lines are so coalesced that it is difficult to distinguish them from each other.

In conclusion, we developed a theoretical model to calculate the emissivity of low density xenon plasmas using a detailed line-by-line method. The fraction of different charge states is determined by solving the completely coupled rate equation with a large number of autoionized states included. In the detailed line-by-line treatment, the

atomic data such as radiative transition probability and electron impact excitation cross section were obtained by large-scale configuration interaction calculations.

Using the developed model, we investigated in detail the emissivity of Xe^{10+} ion at the temperature of 55 eV. The electron density was taken to be 10^{12} cm^{-3}, at which condition Xe^{10+} has the most abundance. It was found that the line intensity is very sensitive to the temperature for dipole forbidden transition lines caused by the transition array of $4s^24p^64d^75s \rightarrow 4s^24p^64d^8$. Such investigations were extended to nearby xenon ions and real plasmas. The results showed that the abundance of different charge states is sensitive to the temperature, resulting in a sensitivity of the emissivity with temperature. Our model is useful to analyze and interpret EBIT experimental observations.

This work was supported by the National Natural Science Foundation of China under Grants Nos. 10774191, 10878024 and 10734140, and the National Basic Research Program of China (973 Program) under Grant No. 2007CB815105.

References

1. G. Kubiak, L. Bernardez, K. Krenz, Proc. SPIE **3331**, 81 (1998)
2. S.S. Churilov, Y.N. Joshi, J. Reader, Opt. lett. **28**, 1478 (2003)
3. S.S. Churilov, Y.N. Joshi, J. Reader, R.R. Kildiyarova, Phys. Scr. **70**, 126 (2004)
4. M.A. Klosner, W.T. Silfvast, J. Opt. Soc. Am. B **17**, 1279 (2000)
5. N. Bowering, M. Martins, W.N. Partlo, I.V. Fomenkov, J. Appl. Phys. **95**, 16 (2004)
6. F. Gilleron, M. Poirier, T. Blenski, M. Schmidt, T. Ceccotti, J. Appl. Phys. **94**, 2086 (2003)
7. E.B. Saloman, J. Phys. Chem. Ref. Data **33**, 765 (2004)
8. K. Fahy, P. Dunne, L. McKinney, G. O'Sullivan, E. Sokell, J. White, A. Aguilar, J.M. Pomeroy, J.N. Tan, B. Blagojevic, E.-O. LeBigot, J.D. Gillaspy, J. Phys. D **37**, 3225 (2004)
9. J.D. Gillaspy, Phys. Scr. **71**, 99 (1997)
10. K. Fahy, E. Sokell, G. O'Sullivan, A. Aguilar, J.M. Pomeroy, J.N. Tan, J.D. Gillaspy, Phys. Rev. A **75**, 032520 (2007)
11. E. Trabert, P. Beiersdorfer, J.K. Lepson, H. Chen, Phys. Rev. A **68**, 042501 (2003)
12. C. Biedermann, P. Radkte, G. Fussmann, J.L. Schwob, P. Mandelbaum, NIM B **235**, 126 (2005)
13. A. Sasaki, K. Nishihara, M. Murakami, F. Koike, T. Kagawa, T. Nishikawa, K. Fujima, T. Kawamura, H. Furukawa, Appl. Phys. Lett. **85**, 5857 (2004)
14. A. Sasaki, T. Kawachi, J. Quant. Spectrosc. Radiat. Transfer **81**, 411 (2003)
15. T. Krucken, K. Bergmann, L. Juschkin, R. Lebert, J. Phys. D **37**, 3213 (2004)
16. A. Bar-Shalom, M. Klapisch, J. Oreg, J. Quant. Spectrosc. Radiat. Transfer **71**, 169 (2001)
17. R. Florido, R. Rodríguez, J.M. Gil, J.G. Rubiano, P. Martel, E. Mínguez, R.C. Mancini, Phys. Rev. E **80**, 056402 (2009)
18. H.-K. Chung, M.H. Chen, W.L. Morgan, Y. Ralchenko, R.W. Lee, High Energy Dens. Phys. **1**, 3 (2005)
19. M.F. Gu, Astrophys. J. **582**, 1241 (2003)
20. A. Burgess, V.B. Sheorey, J. Phys. B **7**, 2403 (1974)